Applied Catalysis B: Environmental 259 (2019) 118034

Contents lists available at ScienceDirect

Applied Catalysis B: Environmental

journal homepage: www.elsevier.com/locate/apcatb

In-situ synthesis of heterojunction TiO_2/MnO_2 nanostructure with excellent performance in vacuum ultraviolet photocatalytic oxidation of toluene

Yingguang Zhang[a], Muyan Wu[a], Y.H. Kwok[a], Yifei Wang[a], Wei Zhao[a], Xiaolong Zhao[a], Haibao Huang[b,*], Dennis Y.C. Leung[a,*]

[a] Department of Mechanical Engineering, The University of Hong Kong, Hong Kong, China
[b] School of Environmental Science and Engineering, Sun Yat-Sen University, Guangzhou, China

ARTICLE INFO

Keywords:
Heterojunction
VUV-PCO
Catalytic ozonation
Ozone decomposition
Photocatalytic mechanism

ABSTRACT

A series of TiO_2/MnO_2 heterojunction catalysts were fabricated through an in-situ hydrothermal method, and for the first time, catalysts with this heterojunction structure were used for VUV-PCO toluene degradation. After the MnO_2 coating, the TiO_2/MnO_2 catalysts performed excellently for both VOCs degradation and residual ozone decomposition with removal efficiency reaching 96.0% and 99.9%, respectively. The enhanced photocatalytic activity towards toluene degradation could be attributed to the heterojunction structure of TiO_2/MnO_2, which provides excellent contact between MnO_2 and TiO_2, and suppresses the recombination of photogenerated electron-hole pairs. Moreover, benefiting from the MnO_2, the ozone generated in the system could be efficiently utilized and eliminated during the VUV-PCO process. The photocatalytic mechanism of TiO_2/MnO_2 for the toluene degradation and ozone decomposition was proposed.

1. Introduction

Volatile organic compounds (VOCs) are known as one of the major hazardous air pollutants including different chemical compounds generated from anthropogenic and natural sources [1]. VOCs in the atmosphere may cause a series of threats to the environment, including the formation of photochemical smog, ozone, and atmospheric PM2.5. In addition, long-term exposure to VOCs may also affect the health of human beings [2,3]. Indoor VOCs, such as formaldehyde, acetone, benzene and toluene, are associated with sick building syndromes including throat irritation, headache and fatigue. It has been proven that some of these airs also raise carcinogenic risk [4]. Therefore, it is crucial to develop efficient ways of removing the VOCs in our environment. Many technologies have been used to control the emission of VOCs, including thermal incineration, physical and chemical adsorption, biological treatment as well as photocatalytic oxidation [5–11]. Among those technologies, photocatalytic oxidation (PCO) of VOCs over metal oxide catalyst is a promising and a low-cost method of removing it at room temperature [12–17].

Recently, vacuum ultraviolet (VUV) photocatalytic oxidation was reported to perform excellently in the degradation of VOCs due to its unique oxidation process. Numerous reactive species of ozone (O_3) and hydroxyl radicals ($^{\cdot}OH$) can be generated under the irradiation of 185 nm UV light. It has been demonstrated that these O_3 and $^{\cdot}OH$ can efficiently decompose the organic intermediates during the reaction, which help reduce the accumulation of the by-products and avoid the deactivation of catalysts, resulting in an enhancement in VOCs degradation performance. Enormous catalysts have been explored for the PCO of VOCs, among which, TiO_2 is widely used due to its high activity, nontoxicity and low cost. It was reported that the photocatalytic activity of TiO_2 relies on both the surface atomic structure and exposure capability to reactive crystal facets

According to theoretical studies, the catalytic activity of {001} surface of anatase TiO_2 nanosheets (NSs) is much higher than that of the {101} surface [5]. The {001} surface of anatase TiO_2 NSs has a surface energy of about 0.98 J m^{-2}, while those of {101} and {100} are only about 0.49 J m^{-2} and 0.58 J m^{-2}, respectively. Yu et al. reported that anatase {001} and {101} facets exhibit different band structures and band edge positions [18]. Under the irradiation of sunlight, photogenerated holes will move from {001} to {101} facets, while electrons will move in the opposite pathway. Therefore, a surface heterojunction will form between the co-exposed {101} and {001} facets, which results in the improvement of the photocatalytic activity [6]. Wang et al. also reported that higher toluene adsorption capacity and degradation performance could be achieved when TiO_2 NSs have a higher ratio of {001} facets [19].

* Correspondence authors.
E-mail addresses: huanghb6@sysu.edu.cn (H. Huang), ycleung@hku.hk (D.Y.C. Leung).

https://doi.org/10.1016/j.apcatb.2019.118034
Received 11 June 2019; Received in revised form 27 July 2019; Accepted 31 July 2019
Available online 03 August 2019
0926-3373/

However, as a by-product in the VUV process, excessive O_3 poses a health hazard that needs to be removed. Unfortunately, TiO_2 alone showed poor ability for O_3 removal, thereby, limiting its application in the VUV-PCO of VOCs. It was reported that O_3 could be decomposed efficiently in the presence of MnO_2 [13,14,20–25]. When modified with MnO_2, MnO_2/TiO_2/ZSM-5 catalyst performed excellently during the utilization as well as elimination of O_3. Nevertheless, the high recombination rate of photogenerated electrons (e^-) and holes (h^+), and the low decomposition efficiency of the by-products, resulting in a limited degradation efficiency of VOCs. Therefore, it is highly desirable to design and synthesize a multifunction catalyst with high efficiency of VOCs degradation as well as O_3 decomposition.

In the present work, MnO_2 was grown in-situ on the surface of TiO_2 [001] NSs through the reaction of $KMnO_4$ with a carbon layer intermediate. Toluene was chosen as the representative VOCs in this study due to its high toxicity. The catalysts were tested in a VUV-PCO system to evaluate their performance in toluene degradation and O_3 elimination. TiO_2 NSs with dominant high-energy {001} facets were fabricated first, a layer of carbon was then coated on the TiO_2 NSs to facilitate the in-situ growth of MnO_2 NSs as schematically depicted in Fig. S1. Combining with a thin layer of MnO_2 on the surface, this novel heterojunction structure of TiO_2/MnO_2 NSs performed excellently in the photocatalytic degradation of toluene, as well as exhibited a dual-function of O_3 utilization and destruction. For the first time, we report this heterojunction nanostructured TiO_2/MnO_2 NSs for the VUV photocatalytic degradation of toluene, which inspires a new approach to design multifunction catalysts that can improve the efficiency of toluene degradation.

2. Experimental

2.1. Materials

Titanium butoxide ($C_{16}H_{36}O_4Ti$) and D-(+)-Glucose monohydrate ($C_6H_{12}O_6{\cdot}H_2O$) were purchased from Aladdin. Potassium permanganate ($KMnO_4$), Sodium sulfate (Na_2SO_4), hydrofluoric acid (HF) and ethanol (C_2H_5OH) were provided by Sigma Aldrich. All the chemicals used were without further purification and DI water (18.2 Ω cm) was used throughout this study.

2.2. Preparation of heterojunction photocatalysts

TiO_2 NSs with dominant {001} facets were fabricated by the hydrothermal method [18]. A total of 25 mL of TBOT was firstly put into a Teflon-lined autoclave, 4.5 mL of HF was then added to the TBOT solution dropwise under stirring for about 30 min. Thereafter the mixture solution was put into an oven and reacted at 180 °C for 24 h. The obtained samples were washed with water and ethanol thrice, then dried at 60 °C overnight, followed by calcination in air at 500 °C for 2 h to remove the F in the TiO_2 NSs.

In preparing TiO_2/MnO_2 NSs, a layer of carbon was firstly coated on the surface of the TiO_2 NSs. 1 g TiO_2 NSs was added into 100 mL of glucose solution (0.04 M) and stirred overnight. After centrifugation and drying, the sample was heat-treated at 500 °C in N_2 gas for 2 h. After the carbon deposition process, the sample was dissolved into 40 mL (0.005 M) $KMnO_4$ solution with drastic stirring for 30 min and kept at 120 °C for 5 h in the oven for in-situ growth of MnO_2. TiO_2/MnO_2 NSs were obtained after washing with distilled water and drying at 60 °C for 12 h. The content of MnO_2 could be adjusted by changing the concentration of $KMnO_4$ solution during the synthesis process, a series of TiO_2/MnO_2 NSs with different percentage of Mn were synthesized and referred to as x-M-T (x = 1, 2, 3, 4, 5).

2.3. Material characterization

As-prepared samples were characterized by scanning electron microscopy (SEM; Hitachi S-4800, 15 kV) equipped with an energy dispersive X-ray spectrometer (EDX), transmission electron microscopy (TEM; Philips CM100), scanning transmission electron microscope (STEM, FEI Tecnai G2 20 S-TWIN), and powder X-ray diffraction (XRD) with Cu Kα radiation at 40 kV and 40 mA (D8 Advance, Bruker). UV–vis diffuse reflectance spectra (UV–vis DRS) was determined on a Varian Cary 5000 Scan UV–vis-NIR spectrometer, with $BaSO_4$ as a reference. Raman spectroscopy was obtained using a HR Evolution Raman microscope (Labram HR800 Evolution) with a laser light of 633 nm. The valence band of Ti, Mn, and O of the as-prepared sample were determined by a Perkin Elmer PHI5000 X-ray photoelectron spectrometer with Al Kα (1486.6 eV) radiation. Photoluminescence (PL) spectra were obtained by a Cary Eclipse Fluorescence Spectrophotometer. Fluorescence spectra were recorded by Edinburgh Instrument FLS920. The photoelectrochemical experiments were carried out using an electrochemical workstation (CHI660E, Shanghai Chenhua Ltd., China) in a

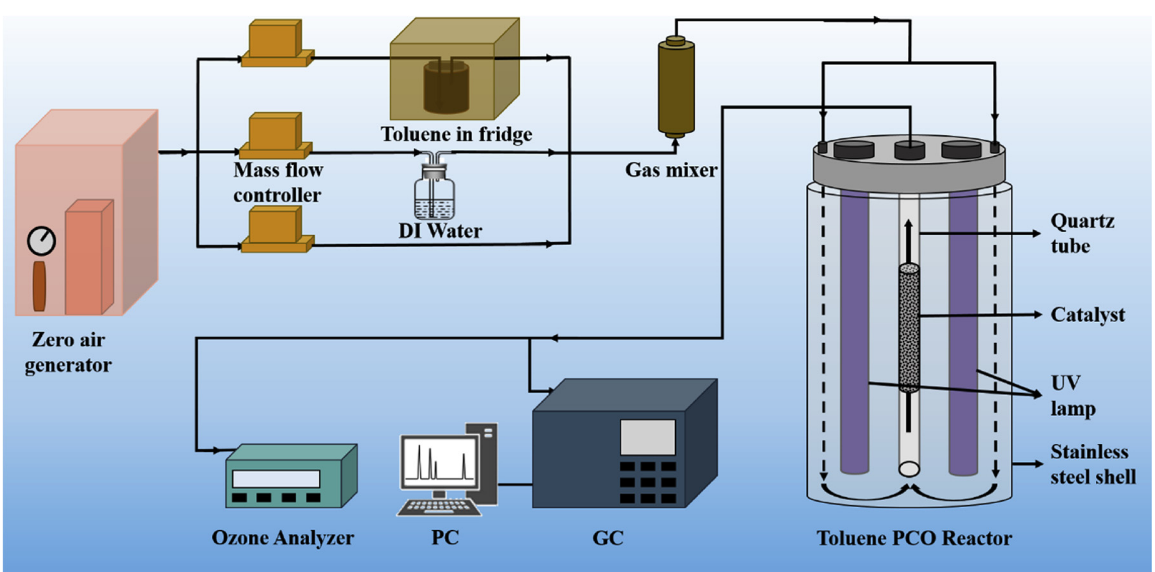

Fig. 1. Schematic diagram of the VUV-PCO set-up.

three-electrode cell, with 0. 2 M Na_2SO_4 aqueous solution as electrolyte.

2.4. Photocatalytic activity test

Photocatalytic degradation of toluene was carried out in a continuous-flow fixed-bed reactor as shown in Fig. 1, which was reported in our previous study [24]. A quartz tube with a diameter of 9 mm was set in the middle of a stainless-steel reactor for catalysts loading, with two VUV lamps (4 W, Cnlight) on either side of the reactor. Toluene was injected into the reactor with an air stream at a flow rate of 1 L/min containing 30 ppm toluene, the humidity of the mixture gases was controlled at 50% (which has been proved to be the best in our previous study [26]). O_3 can reach its highest value (70 ppm) within 2 min under VUV lamps irradiation. The size of the catalysts was controlled at 20–40 mesh by a tablet press, with 1 g of the catalysts used for each test. The photocatalytic degradation tests were performed after purging for about 30 min to minimize the physical adsorption of toluene. The concentrations of outlet gases of toluene, CO and CO_2 at the outlet were detected every 10 min by a gas chromatograph (GC) (9790PLUS, Fuli Instruments, Zhejiang, China,) equipped with two flame-ionization detectors (FID with the detection range of toluene of 0.5 ~ 2500 ppm). The residual O_3 concentration was also examined by an ozone analyzer (202, 2 B Technology). All the experiments were carried out under the same conditions, and the total test time for each experiment was about 200 min. The catalyst was replaced by a fresh sample after each test cycle. Sample stability test was carried out using the same sample after recovering at 180 ℃ for 3 h in an oven. The toluene conversion and O_3 removal efficiency were calculated based on molar basis according to Eqs. (1) and (2), respectively.

$$\text{Toluene conversion }\% = \left(\frac{\text{Toluene}_{[\text{inlet}]} - \text{Toluene}_{[\text{outlet}]}}{\text{Toluene}_{[\text{inlet}]}}\right) * 100\% \tag{1}$$

$$O_3\ \text{ removal efficiency }\% = \left(\frac{O_{3[\text{generate}]} - O_{3[\text{outlet}]}}{O_{3[\text{generate}]}}\right) * 100\% \tag{2}$$

3. Results and discussion

3.1. Structure and morphology

The phase structure and crystallinity of the as-synthesized samples were characterized by XRD and the corresponding phases are shown in Fig. S2. The characteristic peaks at 25.31°, 36.95°, 37.8°, 38.58°, 48.05°, 53.89°, 55.96°, 62.69°, 68.76°, 70.31°, 75.03° and 76.02° can be assigned to {101}, {103}, {004}, {112}, {200}, {105}, {211}, {204}, {116}, {220}, {215} and {301} facets of anatase TiO_2, respectively [27,28]. From the XRD patterns, we can see that all the samples are well-crystallized and the main diffraction of the peaks can be indexed to the anatase TiO_2 with tetragonal structure [JCPDS No. 73-1764] [18,29]. As shown in Fig. S2a, the broad {004} peak and the narrow {200} peak indicate that crystal growth is primarily limited to the [001] axis, resulting in the dominant {001} facet of TiO_2 nanosheets [30]. However, after coating with MnO_2, no significant MnO_2 peak can be observed in all the TiO_2/MnO_2 NSs samples (Fig. S2a). This may be due to the extremely low concentration and amorphous nature of the MnO_2, which was confirmed by EDS as shown in Table S1. However, the diffraction peaks ascribed to anatase TiO_2 phase are weaker with increase in MnO_2 content (Fig. S2b). According to the calculation, the crystallite size of TiO_2 NSs shows a little decline from 28.5 nm of TiO_2 NSs to 25.2 nm of 5-M-T, reflecting that the presence of MnO_2 prevents the crystallization of TiO_2 nanosheets [31].

To investigate the surface compositions and chemical states of the TiO_2/MnO_2 NSs (3-M-T), XPS was carried out as shown in Fig. 2, which exhibits main peaks of O1 s, Mn 2p and Ti 2p on the 3-M-T sample, indicating the presence of Mn. The main O1 s peak position at about 529.40 eV corresponds to lattice oxygen of the Ti-O bond [20]. The Mn 2p XPS spectra exhibits two peaks at about 641.67 eV and 653.78 eV, corresponding to the $Mn2p_{3/2}$ and $Mn2p_{1/2}$, respectively [32]. The ratio of Mn^{3+}/Mn^{4+} was about 0.6 calculated from the areas of the two peaks of Mn 2p, indicating that both MnO_2 and Mn_2O_3 exist in the samples. Since MnO_2 has a large proportion and some reports in literature regarded the material as MnO_2 [33–35], therefore, we interpreted the heterojunction catalyst as TiO_2/MnO_2 in our manuscript. It was reported that the existence of Mn^{3+} will lead to the generation of oxygen vacancies for maintaining electrostatic balance, which can act as active sites during the photocatalytic oxidation process [36–38]. The higher ratio of Mn^{3+}/Mn^{4+} in the sample indicates the higher content of oxygen vacancies. Thus, this high ratio of Mn^{3+}/Mn^{4+} (about 0.6) in the present sample indicates a large amount of oxygen vacancies of TiO_2/MnO_2 NSs, which also means a higher activity for the oxidation of pollutants. In Ti 2p region, the Ti $2p_{1/2}$ and Ti $2p_{2/3}$ main peak positions of TiO_2/MnO_2 NSs occur at 458.83 eV and 464.50 eV, respectively (Fig. 2d).

The morphologies of the as-synthesized samples were characterized by TEM as shown in Fig. 3. The well-defined TiO_2 NSs shows a rectangular outline structure with a side length of about 40 nm and a thickness of about 6 nm, which is in agreement with the report of Yu et al. [18]. After coating with MnO_2, some differences can be observed on the TiO_2 NSs. When the concentration of $KMnO_4$ is very low, almost no MnO_2 can be detected in the TEM image of the 1-M-T sample (Fig. 3b). However, when the concentration of $KMnO_4$ solution increased, a little amount of MnO_2 can be found in the 2-M-T sample (Fig. 3c). Further increase in the concentration of $KMnO_4$ solution leads to the coating of sheet structured MnO_2 on the surface of TiO_2 (001) NSs (Fig. 3d and e). These MnO_2 nanosheets are very thin and can be easily distinguished from TiO_2 (001) NSs. Further increase in the concentration of $KMnO_4$ leads to a corresponding coating of MnO_2 NSs on the surface of TiO_2. However, when MnO_2 reached a certain level, MnO_2 NSs merged together and grew into large particles, as can be seen in Fig. 3f. In the 4-M-T sample, almost all the TiO_2 (001) NSs are coated with MnO_2 NSs, and the excessive MnO_2 NSs appeared in large particles. The contents of MnO_2 NSs in the TiO_2/MnO_2 NSs samples were detected by the EDS as shown in Table S1. Only about 0.15 wt.% of Mn was observed in the 1-M-T sample, which increased with further increase in $KMnO_4$ concentration during the synthesis and reached about 1.59 wt.% for the 5-M-T sample.

The SEM images of TiO_2 and the 3-M-T sample are shown in Fig. S3 displaying the morphology of the catalysts. These two catalysts showed nanosheet structures with relatively large thickness, which may be due to the calcination for removing the F ion. However, after coating with MnO_2, some thin nanosheets can be observed on the surface of TiO_2 NSs, which can be assigned to MnO_2 NSs and agrees with the TEM images mentioned above. To acquire more information about the morphology of the photocatalyst, high-resolution TEM (HRTEM) and mapping were performed on the 3-M-T sample (Fig. 4). The side view of TiO_2 NSs is shown in Fig. 4b and the inset figure displays a d-spacing of about 0.235 nm, corresponding to (004) anatase crystalline phase that agrees well with the literature [19,39].The TEM-EDX mapping of the 3-M-T sample shows the presence of Ti, O and Mn elements, indicating uniform distribution of Mn on the TiO_2 NSs.

3.2. Optical properties

UV-vis absorption spectra obtained from the TiO_2 NSs and TiO_2/MnO_2 NSs with different loading amounts are compared and shown in Fig. 5a. The as-prepared TiO_2 NSs displayed an absorption edge of about 410 nm. After coating with MnO_2, all the TiO_2/MnO_2 NSs samples showed a decline in the area of UV region absorption (about 200–340 nm). This may be due to the fact that the MnO_2 NSs prevents the light absorption of TiO_2. However, the absorption range of TiO_2/MnO_2 NSs was extended from 410 nm to near infrared light (800 nm).

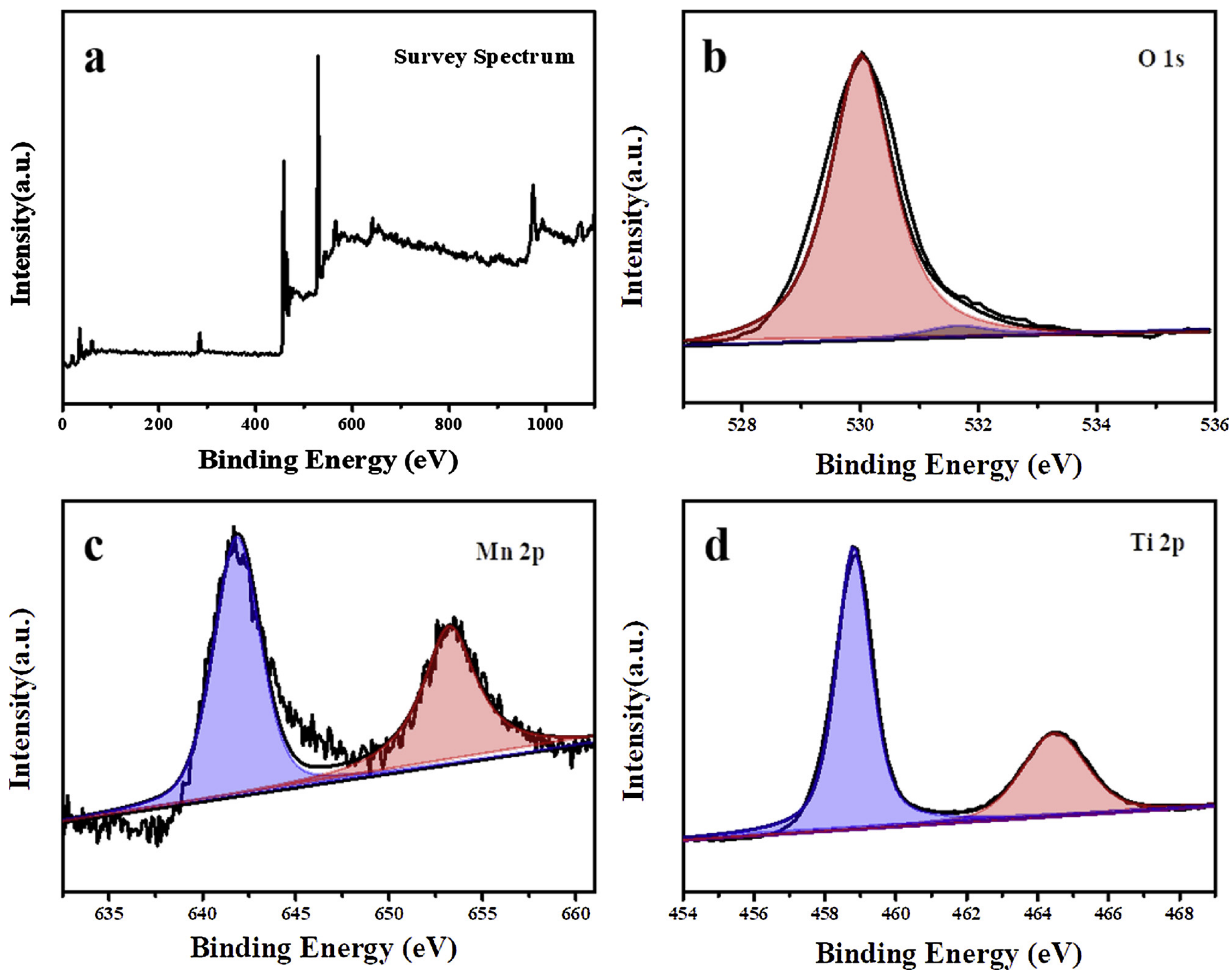

Fig. 2. (a) XPS spectrum of the as-prepared samples of 3-M-T, XPS spectra of (b) O 1s, (c) Mn 2p and (d) Ti 2p peaks of 3-M-T.

This significant extension of light absorption may be due to the narrow bandgap of MnO_2 [40]. In addition, light absorption intensity of TiO_2/MnO_2 NSs in visible light region increased with increase in the proportion of MnO_2. The band gap energy (E_g) of the samples were calculated by the Kubleka-Munk method (Eq. 3) as follows: [41]

$$\alpha h\upsilon = A(h\upsilon - E_g)^2 \tag{3}$$

As shown in Fig. 5b, the Eg value of TiO_2 is about 3.0 eV. After coating with MnO_2, the E_g value of the 3-M-T sample is about 2.25 eV, confirming the re-shift in the TiO_2/MnO_2 heterojunction compared with pristine TiO_2 NSs.

The phase compositions of the TiO_2 and TiO_2/MnO_2 NSs were investigated by Raman spectroscopy. Fig. 5c shows the fundamental Raman spectra of the samples. The 4 main peaks, observed at 145 cm^{-1} (E_g mode), 396 cm^{-1} (B_{1g} mode), 518 cm^{-1} (A_{1g} mode), and 640 cm^{-1} (E_g mode), were all due to TiO_2 [42]. The peak observed at 572 cm^{-1} was attributed to Mn-O stretching in the basal plane of MnO_6 sheets [43,44]. It can be seen that, after coating with MnO_2 nanosheets, the intensity of the E_g peaks at 145 cm^{-1} and 640 cm^{-1} decreased slightly, while the intensity of both the B_{1g} peak (at 396 cm^{-1}) and A_{1g} peak (at 518 cm^{-1}) showed a significant reduction. It is reported that the E_g peak is mainly caused by symmetric stretching vibration of O—Ti—O in TiO_2, the B_{1g} peak is caused by symmetric bending vibration of O—Ti—O, while the A_{1g} peak is caused by antisymmetric bending vibration of O—Ti—O [23]. The percentage of the exposed anatase TiO_2 (001) facets has a direct relationship with the intensity variations of the Raman vibrational mode of the E_g and A_{1g} peaks [44].

PL spectra of the samples were obtained to investigate the carriers' separation efficiency. As shown in Fig. S4a, the PL quantum yield of the TiO_2/MnO_2 heterojunction was greatly reduced compared with that of the pristine TiO_2, demonstrating an enhanced charge carriers' separation and reduced recombination. The time-based florescence spectra further confirmed the efficient charge carriers' separation over the 3-M-T sample (Fig. S4b). The average lifetime of the carriers (τ_{avg}) is about 2.07 ns for the 3-M-T sample, which is much longer than that of the pristine TiO_2 (about 0.69 ns). The increased τ_{avg} can be attributed to the formation of heterojunction that prolong the lifetime of the photogenerated charges.

3.3. Electrochemistry properties

To analyze the separation and migration efficiency of the photogenerated electrons and holes of the samples, photoelectrochemical measurements were carried out using an electrochemical workstation and the results are shown in Fig. 6. Typical i–t curves for the as-prepared electrodes of TiO_2 and 3-M-T samples were obtained using a 0.2 M Na_2SO_4 solution as electrolyte at a constant bias voltage of 0.8 V vs. SCE under the irradiation of two VUV lamps. The photocurrent density of pristine TiO_2 NSs is about 3.8 μA/cm^2, while the photocurrent density of the mixture of TiO_2 NSs with MnO_2 is slightly higher than that of the pristine TiO_2. However, after coating with MnO_2, the photocurrent density of the 3-M-T sample increased to about 6.2 μA/cm^2 under the same condition (Fig. 6a). This enhancement of photocurrent density indicated the efficient separation promotion of

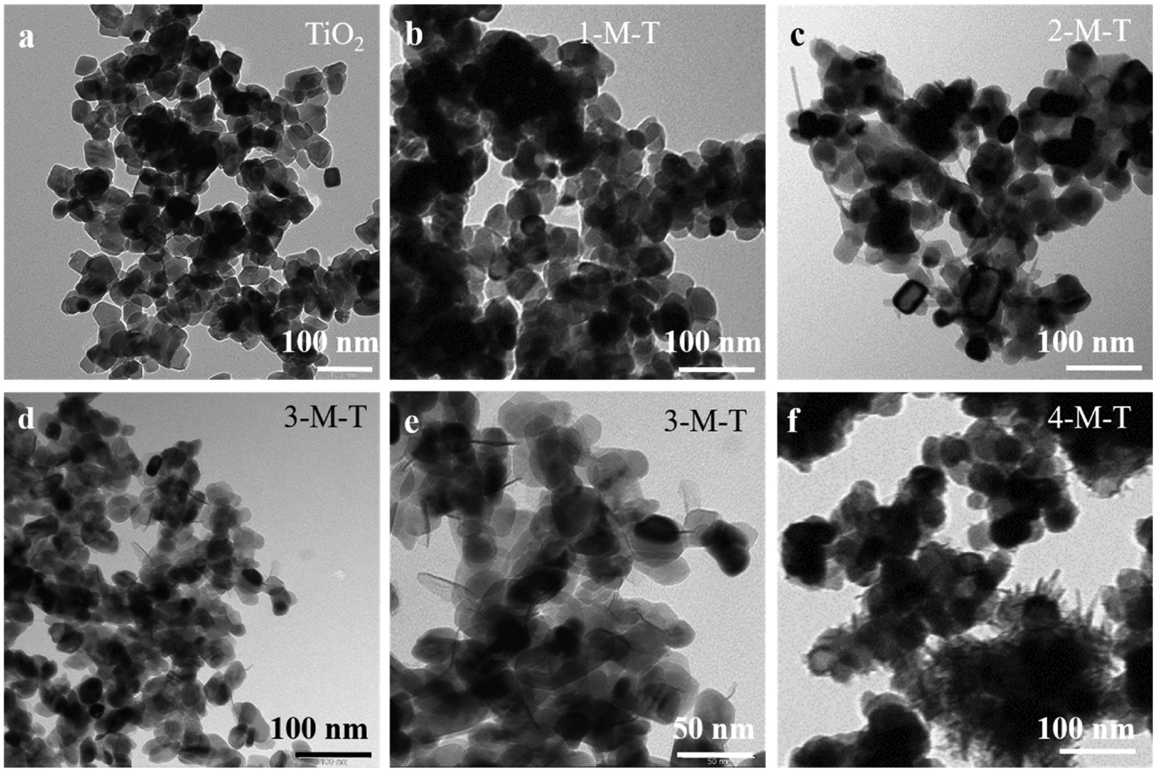

Fig. 3. TEM images of TiO_2 NSs and TiO_2/MnO_2 NSs.

photogenerated charge carriers and inhibition of the recombination of electron-hole pairs. After coating with MnO_2, heterojunction structure was constructed over the TiO_2/MnO_2 sample, which enhanced the transfer of photogenerated charge carriers. Under the irradiation of VUV light, the electrons generated by the excited state of TiO_2 will be transferred to the conduction band of MnO_2, resulting in an effective separation and migration of photogenerated electron-hole pairs [40].

The electrochemical impedance spectroscopy (EIS) measurements were carried out to study the interfacial properties of the photocatalysts as shown in Fig. 6b. The EIS was conducted in the frequency range of $10^4 \sim 10$ Hz using an amplitude of 5 mV at the open circuit potential of the system. The semicircle of the Nyquist plots at high frequencies showed the characteristic of the charge transfer process of the photocatalysts. Smaller diameters indicate lower charge-transfer resistance of the sample. It is clear that the 3-M-T heterojunction catalyst exhibited the smallest diameter among all the samples, indicating the lowest charge transfer resistance, and hence, the lowest recombination rate of the photogenerated electron-hole pairs [18,45].

Mott-Schottky measurements were carried out to investigate the electronic structure of the as-prepared samples. The Mott-Schottky plots of the samples were measured at 1000 Hz versus Ag/AgCl electrode. The carrier density (N_D) of the samples can be obtained by the following Mott-Schottky Eq.

$$\frac{1}{C^2} = \frac{2}{e\varepsilon_r\varepsilon_0 N_D A^2}\left(E - E_{fb} - \frac{kT}{e}\right) \quad (4)$$

where C is the space charge capacitance, E is the applied potential, e is the electron charge, k is the Boltzmann constant, T is the absolute temperature, A is the active area of the electrode, E_{fb} is the flat-band potential, ε_r and ε_0 are the semiconductor and free space dielectric constant, respectively [46,47]. As shown in Fig. 6c, the E_{fb} for the TiO_2 and 3-M-T are -0.51 V and -0.58 V (vs. Ag/AgCl), respectively. The N_D calculated from the slope of the linear region for TiO_2 and 3-M-T samples are 5.27×10^{18} cm^{-3} and 6.31×10^{18} cm^{-3}, respectively. The higher carrier density of the 3-M-T sample than that of pristine TiO_2 sample indicates the enhanced charge transport. This result confirms that the formation of heterojunction in the 3-M-T sample could result in a higher photocatalytic activity in VOCs degradation.

3.4. Photocatalytic activity

Toluene removal efficiencies over different as-synthesized samples under the VUV-PCO process are shown in Fig. 7. As can be seen, the photolysis efficiency of toluene degradation in the VUV-PCO system is about 69.4%, which increased to 77.8% with the additional use of TiO_2 NSs photocatalysts due to the catalytic effect of TiO_2 under light irradiation. However, with increase in testing time, the removal efficiency of TiO_2 NSs showed a decline from 82.5% to about 76.0%, which may be due to the accumulation of by-products on the surface of TiO_2 [40]. However, after coating with MnO_2, the toluene removal efficiency of the 1-M-T heterojunction catalyst reached 93.5%. Moreover, when the content of Mn in the composite catalysts increased from 0.15% (1-M-T) to 0.67% (3-M-T), the toluene removal efficiency reached its highest value of about 96.0% (3-M-T). This excellent performance of the TiO_2/MnO_2 NSs illustrated that the introduction of MnO_2 during the VUV-PCO process can help to decompose the by-products on the surface of TiO_2. On the other hand, MnO_2 on the photocatalysts surface can also effectively utilize the O_3 produced by the VUV light irradiation to further decompose the toluene in the exhaust. However, when the content of Mn further increased, i.e. 1.19% (4-M-T) and 1.75% (5-M-T), the toluene removal efficiency dropped to about 89.3% and 85.2%, respectively. This means that the content of MnO_2 has the optimum value, at about 0.67% for the TiO_2/MnO_2 NSs catalysts. The lower activity at the high MnO_2 level may be due to the fact that too much MnO_2 coated on the surface of TiO_2 NSs will reduce the light absorption and block the active sites of TiO_2, leading to a lower photocatalytic activity for the degradation of toluene over TiO_2.

To investigate the degree of mineralization, the outlet CO_x concentration generated during the VUV-PCO process was measured by GC. The concentration of CO and CO_2 generated from toluene degradation

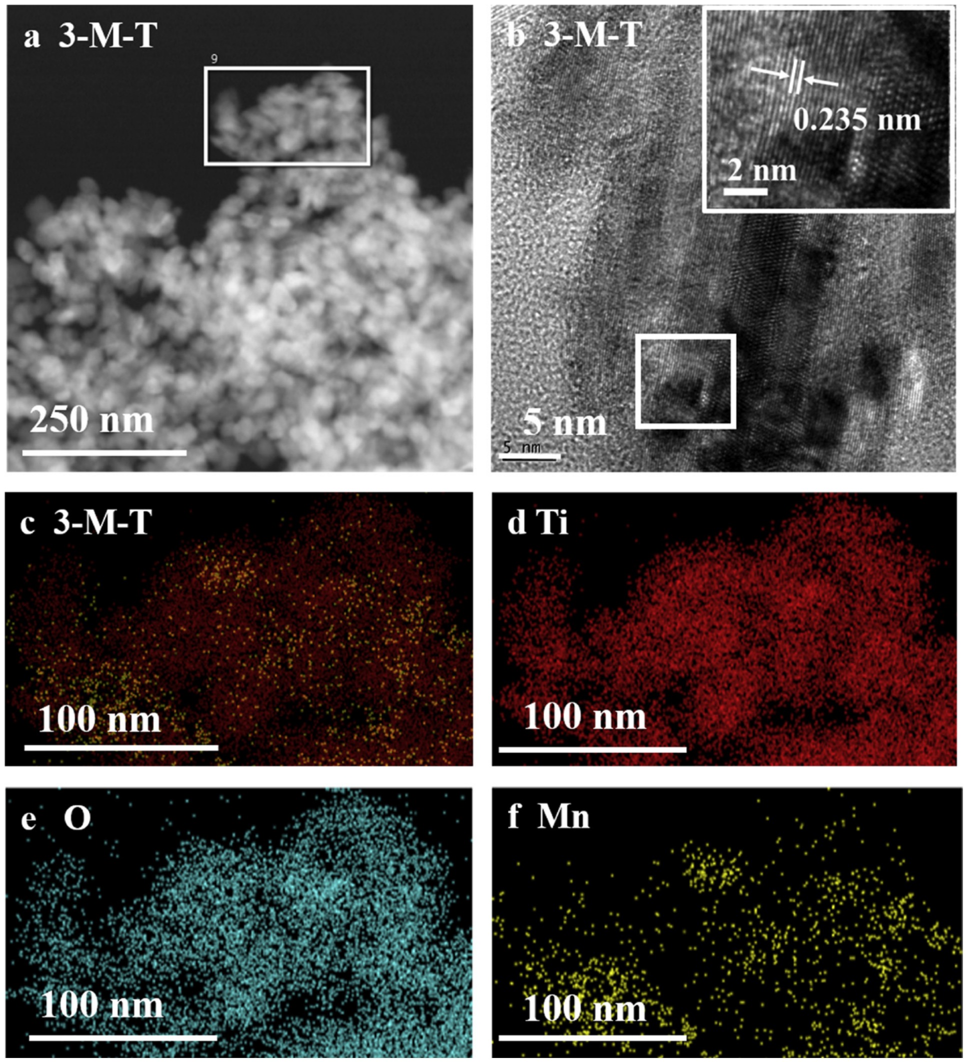

Fig. 4. (a,b) HRTEM images of 3-M-T and (c–f) corresponding mapping images of Ti, O and Mn.

over different catalysts were shown in Fig. 8. Both CO_2 and CO can be detected after the degradation of toluene. The concentration of CO and CO_2 for pristine TiO_2 was about 23 ppm and 45 ppm, respectively, which is a little lower than that of the simply photolysis process. This may be due to the by-products accumulation on the surface of TiO_2 because of its weak ability to decompose them. After coating with MnO_2, the CO concentration showed an increase over all the TiO_2/MnO_2 NSs catalysts. It reached 34 ppm after coating a small amount of MnO_2 over the 1-M-T sample (Mn = 0.15 wt.%). However, the CO concentration showed a decreasing trend with increase in the content of MnO_2, and decreased to about 27 ppm for the 5-M-T sample (Mn = 1.75 wt.%). On the contrary, the outlet CO_2 generated from toluene degradation showed a significant improvement after coating with MnO_2. At first, the CO_2 concentration increased with increasing content of MnO_2 in the TiO_2/MnO_2 NSs. However, after reaching its maximum at about 74 ppm (3-M-T and 4-M-T), the CO_2 generated from toluene degradation decreased to about 69 ppm for the 5-M-T sample, showing a similar trend as the toluene degradation (Fig. 8a). In conclusion,

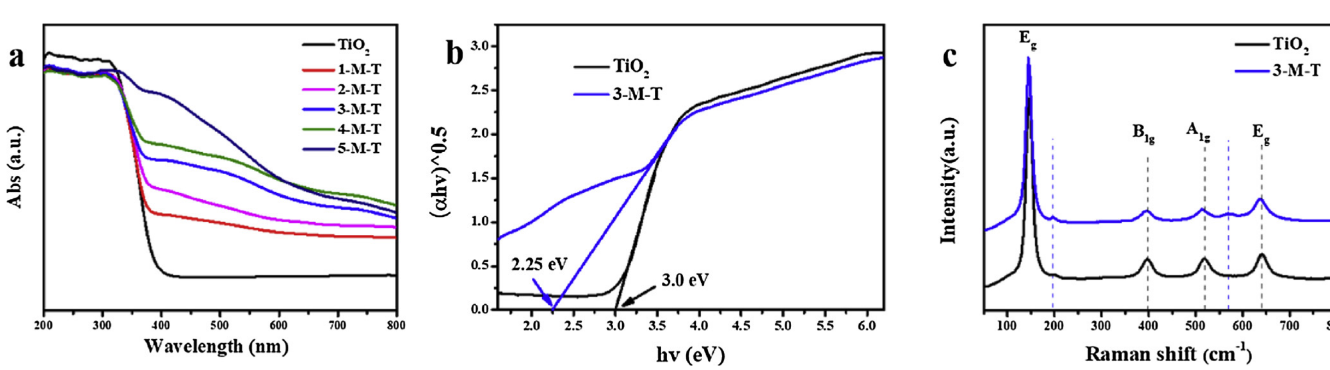

Fig. 5. (a) UV–vis absorbance spectra patterns of as-prepared samples, (b) the plot of $(ah\nu)^{0.5}$ vs. energy $h\nu$ and energy band gap of TiO_2 and 3-M-T, (c) Raman shift of TiO_2 and 3-M-T.

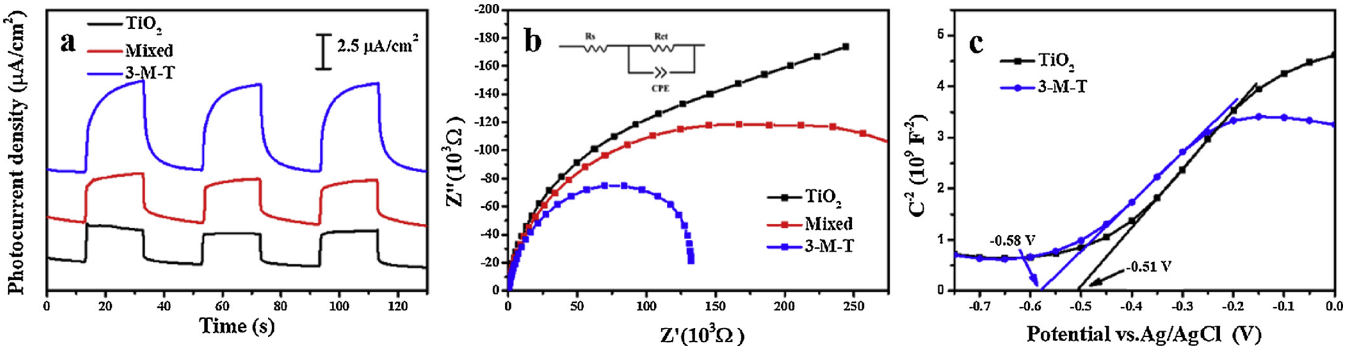

Fig. 6. Electrochemical properties of as-prepared samples, (a) Photocurrent density of TiO_2, mixed (TiO_2 NSs and MnO_2) and 3-M-T, (b) Nyquist plots and (c) Mott–Schottky plots of TiO_2 and 3-M-T.

owing to the catalytic ozonation effect provided by MnO_2 and the synergistic effect of VUV-PCO, this heterojunction TiO_2/MnO_2 nanostructure composites showed an excellent performance for toluene degradation and mineralization.

To investigate the effect of O_3 on toluene degradation in the VUV-PCO process, we measured the residual O_3 concentration over different catalysts using an ozone analyzer and the result is shown in Fig. 9. Under the irradiation of VUV light, the O_3 generated in the system was regarded to be the same since the same VUV lamps were used for all the tests. First, we measured the O_3 concentration over the photolysis, which was used as a standard to calculate the O_3 removal efficiency for all the catalysts. Previous work has proved that irradiated TiO_2 can act as an active center for O_3 decomposition into O_2 and O^- [48]. As shown in Fig. 9, the O_3 removal efficiency of TiO_2 (001) NSs was only about 11.7%, showing its poor ability to decompose O_3. However, after coating with MnO_2, almost all the residual O_3 has been decomposed over the TiO_2/MnO_2 heterojunction catalysts. All the O_3 decomposition efficiency over TiO_2/MnO_2 NSs with different Mn percentage were about 99.7%, indicating that the introduction of MnO_2 can greatly promote the O_3 decomposition, which can be due to the active sites provided by Mn for catalytic oxidation of O_3. In the VUV-PCO process, both the O_3 decomposition and toluene degradation have been improved after the coating of MnO_2, which means that the Mn is crucial for toluene degradation via ozone-assisted catalytic oxidation. Therefore, TiO_2/MnO_2 heterojunction catalysts exhibited multi-functions in the VUV-PCO system. The toluene removal efficiency can reach 96% and almost all the O_3 by-product can be effectively utilized or eliminated during the toluene degradation process. Table 1 summarized the literature data on VOCs photocatalytic degradation over various TiO_2-based catalysts [26,49–54].

In order to test the stability of TiO_2/MnO_2 NSs, we increased the testing time of the VOCs degradation. As shown in Fig. 10a, the VOCs removal efficiency was about 95% at the beginning, which was slightly raised to about 96% after 3 h testing, and remained rather stable after 6 h. Thereafter, we investigated the regeneration ability of this catalyst and the result is shown in Fig. 10b. Calcination was carried out at 180 °C for 3 h to remove the by-products on the surface of the catalyst after the 3 h testing, and the same catalyst was used for the toluene degradation test. As shown in Fig. 10b, the 3-M-T sample showed a stable toluene removal efficiency during the whole 5-cycle tests. Even though it showed a slight fluctuation, the toluene removal efficiency was still maintained at about 96% throughout the 5 cycles tested. This result indicates that the TiO_2/MnO_2 NSs has a high stability for the VUV-PCO of toluene.

To confirm the advantages of this heterojunction structure of the TiO_2/MnO_2 heterojunction catalysts, comparison experiments have been conducted as shown in Fig. 11a. The performance of TiO_2/MnO_2 heterojunction, and a mixture of MnO_2 nanoparticles and the TiO_2 NSs with the same amount of MnO_2 were evaluated. As shown in the figure, the toluene removal efficiency of the mixture is only about 83%, which is much lower than that of the TiO_2/MnO_2 heterojunction (about 96%), indicating that the heterojunction structure of the catalyst promoted the catalytic efficiency in the VUV-PCO toluene degradation due to the increased contact area between TiO_2 and MnO_2 interface. As demonstrated in Fig. 6, the heterojunction structure facilitates the separation and migration of the photogenerated electrons and holes, thus, enhancing the photocatalytic activity of toluene degradation.

To evaluate the effect of hydroxyl radicals in the degradation of toluene under the VUV-PCO process, tert-butanol (TBA) was used as a scavenger for hydroxyl radicals ($^{\cdot}OH$). 10 mM TBA was added dropwise

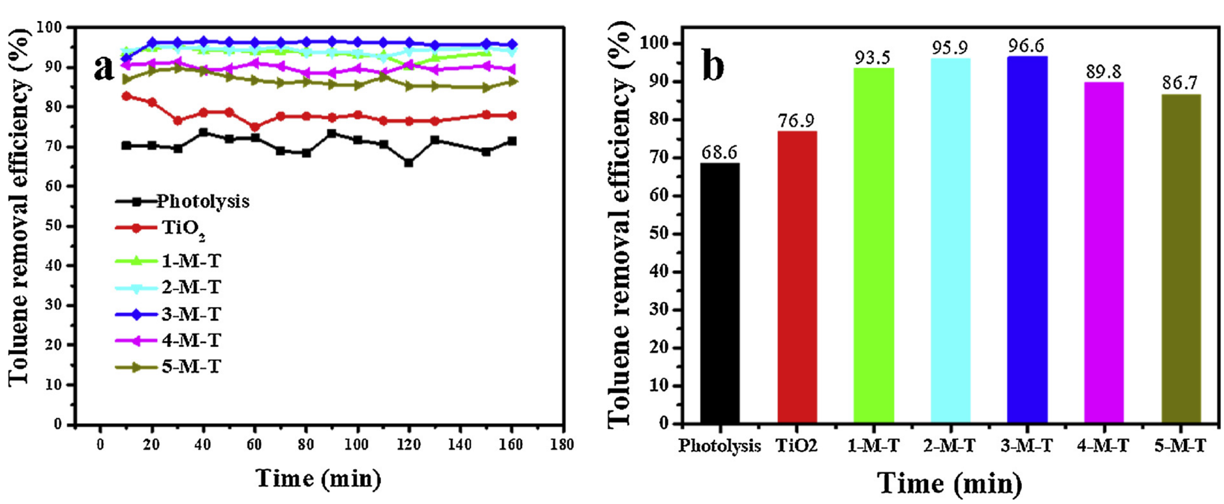

Fig. 7. Photocatalytic degradation of Toluene performance of Photolysis, TiO_2 NSs and TiO_2/MnO_2 NAs.

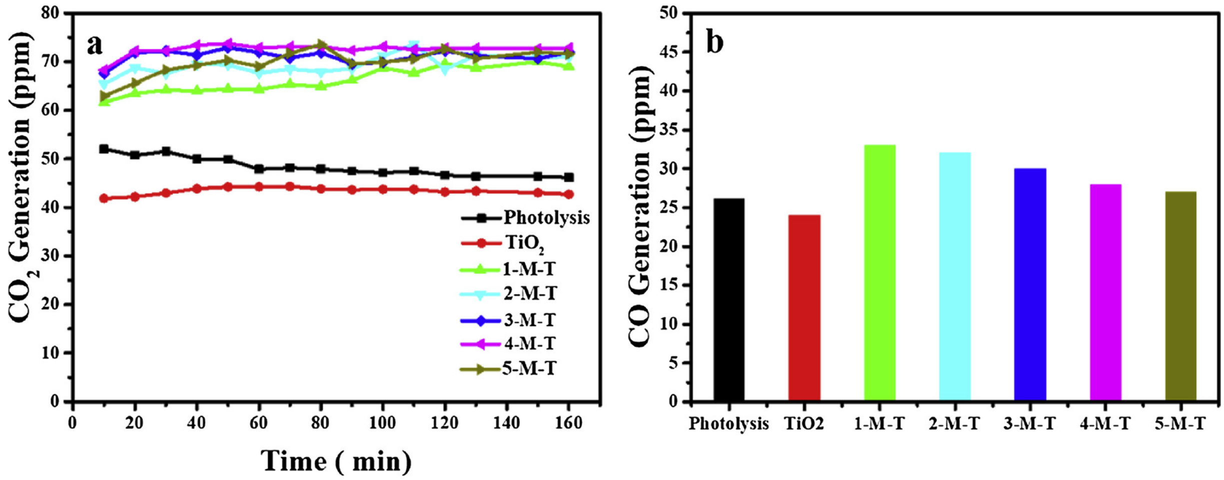

Fig. 8. Outlet CO_2 and CO concentration of different catalysts in VUV-PCO of Toluene.

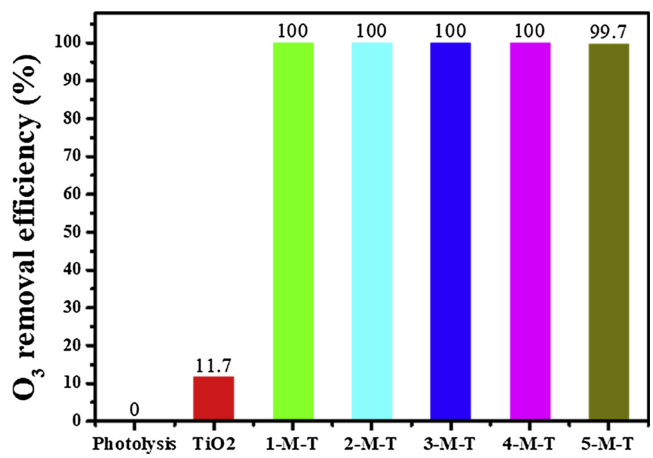

Fig. 9. O_3 removal efficiency of TiO_2 NSs and TiO_2/MnO_2 NSs in the VUV-PCO system.

to the as-prepared 3-M-T sample, and then toluene degradation performance of the catalyst was measured. The results of the toluene removal of the 3-M-T sample and the TBA treated 3-M-T sample are shown in Fig. 11b. It was found that the toluene removal efficiency of the 3-M-T sample decreased from about 96% to 80% after the treatment with TBA, which means the presence of TBA had a negative effect on the degradation of toluene. This result indicated that hydroxyl radicals has critical effect on the VUV-PCO toluene degradation system, which is in-line with our previous study [24].

3.5. Scheme of toluene degradation in VUV-PCO process

Compared with PCO, the VUV-PCO process provides more pathways for the toluene degradation. Under the irradiation of VUV lamp, all of the PCO, photolysis and ozone catalytic oxidation (OZCO) can be well complemented with each other and have a synergistic effect for toluene oxidation. In the VUV-PCO system, besides the UVC (245 nm), there are also VUV (185 nm) irradiation from the VUV lamp that can generate hydroxyl radicals ($^{\cdot}OH$) and ozone. Under the irradiation of 185 nm VUV light, the oxygen and water in the air will react with the energetic photons and dissociate into oxygen species, including $^{\cdot}OH$, $O(^1P)$ and $O(^3P)$. Then, the oxygen in the air can react with $O(^3P)$ species to generate ozone via the following steps (a–e) [20,21,55,56].

a) $H_2\,O \xrightarrow{hv\,(185\,nm)} H+\ \bullet OH$
b) $O_2 \xrightarrow{hv\,(185\,nm)} O(^1D) + O(^3P)$
c) $O(^1D) + M \rightarrow O(^3P) + M\ (M = O_2 \text{ or } N_2)$
d) $O(^3P) + O_2 + M \rightarrow O_3 + M$
e) $O(^1D) + H_2\,O \rightarrow 2\bullet OH$

According to Fig. 6, the introduction of MnO_2 also accelerates the separation of electron-hole pairs, which enhances the toluene degradation. TiO_2 had limited effect on O_3 decomposition. However, after coating with MnO_2, TiO_2/MnO_2 heterojunction catalyst performed excellently in the elimination of O_3, indicating that O_3 generated in the first step could be utilized and decomposed on the active center of MnO_2 via ozone catalytic oxidation of toluene. Taking all the above results into consideration, the possible photocatalytic mechanism of toluene degradation in the VUV-PCO process over TiO_2/MnO_2 heterojunction is proposed as shown in Fig. 12. Under the irradiation of the VUV light, electrons and holes can be generated on the TiO_2 semiconductor. Based on the band energy structure, the conduction band (CB) position of MnO_2 is higher than that of TiO_2 (-0.29 eV). Therefore, under the irradiation of VUV light, the photo-induced electrons of TiO_2 can be transferred to the CB of MnO_2. However, O_2 cannot be reduced to $^{\cdot}O_2^-$ (-0.33 eV) due to the positive CB edge position of MnO_2 (1.33 eV) [57]. Fortunately, the O_3 generated in the first step can act as

Table 1
Literature data on VOCs photocatalytic degradation over various TiO_2-based catalysts.

Catalyst	Light source	Target pollutant	Concentration	Efficiency	Reference
$Pd\text{-}TiO_2$	UV-LEDs 100 W	Benzylic alcohols	0.1mmol	92%	[42]
$Pt\text{-}TiO_2$	UVA-LEDs	Cyclohexane	200 ppm	68%	[43]
$Ag\text{-}TiO_2$	UV 8W	Toluene	120 ppm	98%	[44]
$Cu\text{-}TiO_2$	Light bulb 20 W	Benzene	100 ppm	86%	[45]
$Mn\text{-}TiO_2$	UVC & VUV	Benzene	50 ppm	58%	[46]
$Ni\text{-}TiO_2$	UVC 10W	p-Xylene	80 ppm	60%	[47]
$Fe\text{-}TiO_2$	UV light	Toluene	0.1 ppm	63%	[48]
TiO_2/MnO_2	VUV 4 W	Toluene	30 ppm	96%	This work

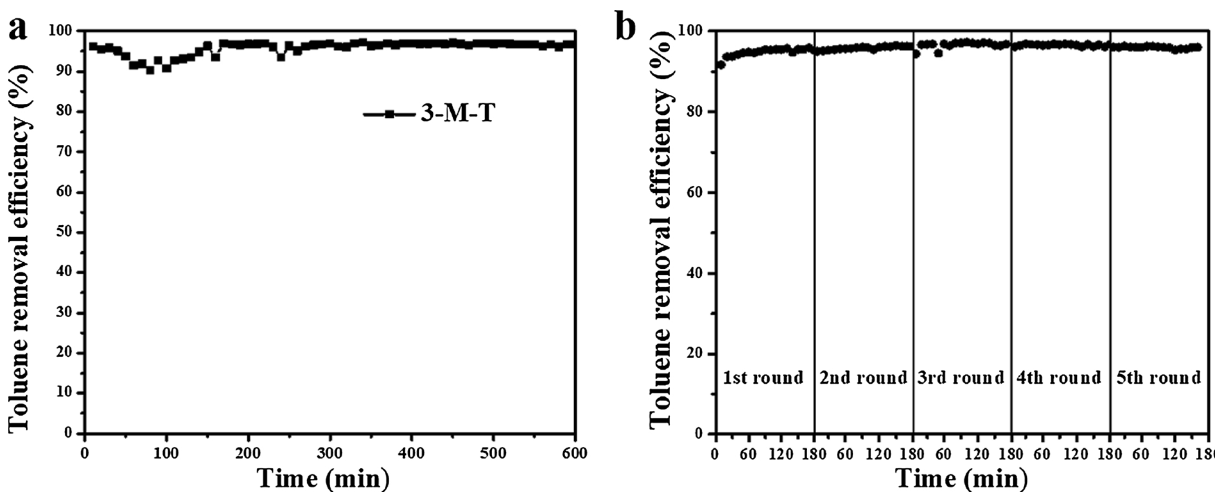

Fig. 10. (a) Stability and (b) regenerated ability of 3-M-T for VUV-PCO degradation of Toluene.

a good electron acceptor and reduced to $^{\cdot}O_3^-$ radicals, which can prevent the recombination of electron-hole pairs [20,58,59]. Meanwhile, the adsorbed H_2O could be oxidized by the $^{\cdot}O_3^-$ radicals to form $^{\cdot}OH$ radicals. Moreover, $^{\cdot}O_3^-$ radicals can oxidize toluene with a relatively long lifetime according to the literature [60]. On the other hand, the holes left in the valance band (VB) of TiO_2 could oxidize OH^- to form $^{\cdot}OH$ radicals.

In addition, Zhang et al. indicated that catalytic ozone decomposition is associated with oxygen vacancies(V_O) [61]. First, the oxygen vacancies transfer two electrons to an O atom of an O_3 molecule that bounded on the TiO_2/MnO_2 heterojunction surface, the O_3 can then be decomposed into an oxygen species (O^-) and a bridging O_2 dimer. The O^- can further react with another O_3 molecule to release an O_2 and a peroxide species (O_2^-). After that, the generated O_2^- reacts with H_2O to generate $^{\cdot}OH$ radicals for toluene degradation. Finally, the generated O_2^- can be decomposed to release an oxygen molecule, and at the same time, V_O is recovered and can participate in the next cycle to decompose O_3 [62,63]. Therefore, the catalytic decomposition of toluene and O_3 on TiO_2/MnO_2 NSs involved in the VUV-PCO process occurs via the following two phases:

Phase I:

a) $TiO_2 \xrightarrow{hv} e^- + h^+$
b) $h^+ + H_2O \rightarrow \bullet OH + H^+$
c) $O_3 + e^- \rightarrow \bullet O_3^-$
d) $\bullet O_3^- + H_2O \rightarrow \bullet OH + OH^- + O_2$

Phase II:

a) $O_3 + V_O \rightarrow O^- + O_2$
b) $O_3 + O^- \rightarrow O_2^- + O_2$
c) $O_2^- + H_2O \rightarrow 2\bullet OH$
d) $O_2^- \rightarrow O_2 + V_O$

Overall, under the irradiation of VUV light and taking advantage of the photocatalytic effect of TiO_2 NSs as well as the catalytic ozonation of Mn, the TiO_2/MnO_2 heterojunction catalyst exhibited multi-functions for efficient toluene degradation and decomposition of all the residual O_3 in the VUV-PCO process.

4. Conclusions

The heterojunction structure of TiO_2/MnO_2 NSs was developed and tested for toluene degradation in the VUV-PCO process. The toluene removal efficiency can reach 96% and almost all the residual ozone can be removed over the TiO_2/MnO_2 heterojunction catalyst under the irradiation of VUV light. The high performance of toluene degradation of the catalyst can be attributed to the introduction of MnO_2 to the surface of the TiO_2 NSs, which enhanced the light absorption ability and inhibited the recombination of photo-induced electron-hole pairs, thus, leading to an enhanced photocatalytic activity for toluene degradation. In addition, the catalytic ozonation of Mn can effectively utilize the generated O_3 to improve the efficiency of toluene degradation in the

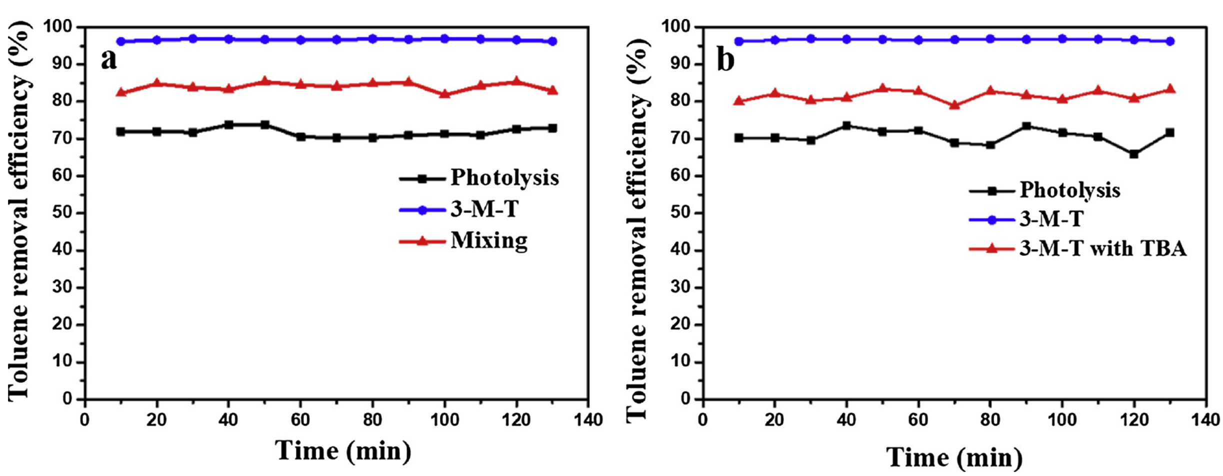

Fig. 11. Toluene degradation performance of the as-prepared samples of (a) TiO_2 NSs mixed with MnO_2 and (b) 3-M-T with TBA.

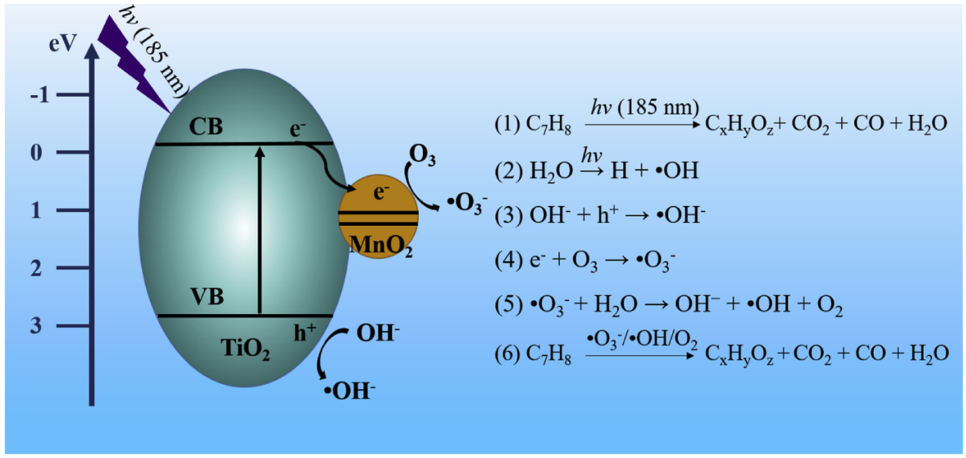

Fig. 12. Schematic diagram of the photocatalytic mechanism of toluene degradation under the VUV-PCO process over TiO_2/MnO_2 heterojunction catalyst.

VUV-PCO process, as well as the elimination of residual ozone in the system. This work provides a new way of developing photocatalysts with high efficiency for VOCs degradation.

Declaration of Competing Interest

The authors declare that they have no known competing financial interests or personal relationships that could have appeared to influence the work reported in this paper.

Acknowledgement

The authors gratefully acknowledge the financial supports from The National Natural Science Foundation of China (NSFC) and The Research Grants Council (RGC) of Hong Kong Joint Research Scheme (No. 51561165015 and No. N_HKU718/15), Hong Kong Innovation and TechnologyGHP/025/16GD & InP/272/16).

Appendix A. Supplementary data

Supplementary material related to this article can be found, in the online version, at doi:https://doi.org/10.1016/j.apcatb.2019.118034.

References

[1] R. Atkinson, Atmospheric chemistry of VOCs and NO x, Atmos. Environ. 34 (2000) 2063–2101.
[2] T. An, Y. Huang, G. Li, Z. He, J. Chen, C. Zhang, Pollution profiles and health risk assessment of VOCs emitted during e-waste dismantling processes associated with different dismantling methods, Environ. Int. 73 (2014) 186–194.
[3] J.K. Holopainen, J. Gershenzon, Multiple stress factors and the emission of plant VOCs, Trends Plant Sci. 15 (2010) 176–184.
[4] H. Guo, S. Lee, L. Chan, W. Li, Risk assessment of exposure to volatile organic compounds in different indoor environments, Environ. Res. 94 (2004) 57–66.
[5] B. Ozturk, D. Yilmaz, Absorptive removal of volatile organic compounds from flue gas streams, Process. Saf. Environ. Prot. 84 (2006) 391–398.
[6] F. Qu, L. Zhu, K. Yang, Adsorption behaviors of volatile organic compounds (VOCs) on porous clay heterostructures (PCH), J. Hazard. Mater. 170 (2009) 7–12.
[7] S. Scire, S. Minico, C. Crisafulli, C. Satriano, A. Pistone, Catalytic combustion of volatile organic compounds on gold/cerium oxide catalysts, Appl. Catal. B Environ. 40 (2003) 43–49.
[8] W.-H. Chen, W.-B. Yang, C.-S. Yuan, J.-C. Yang, Q.-L. Zhao, Fates of chlorinated volatile organic compounds in aerobic biological treatment processes: the effects of aeration and sludge addition, Chemosphere 103 (2014) 92–98.
[9] H. Huang, P. Hu, H. Huang, J. Chen, X. Ye, D.Y. Leung, Highly dispersed and active supported Pt nanoparticles for gaseous formaldehyde oxidation: influence of particle size, Chem. Eng. J. 252 (2014) 320–326.
[10] S.B. Kim, S.C. Hong, Kinetic study for photocatalytic degradation of volatile organic compounds in air using thin film TiO2 photocatalyst, Appl. Catal. B Environ. 35 (2002) 305–315.
[11] G. Moussavi, M. Mahdavianpour, The selective direct oxidation of ammonium in the contaminated water to nitrogen gas using the chemical-less VUV photochemical continuous-flow reactor, Chem. Eng. J. 295 (2016) 57–63.
[12] C. Bianchi, S. Gatto, C. Pirola, A. Naldoni, A. Di Michele, G. Cerrato, V. Crocellà, V. Capucci, Photocatalytic degradation of acetone, acetaldehyde and toluene in gas-phase: comparison between nano and micro-sized TiO2, Appl. Catal. B Environ. 146 (2014) 123–130.
[13] A. Kontos, A. Katsanaki, T. Maggos, V. Likodimos, A. Ghicov, D. Kim, J. Kunze, C. Vasilakos, P. Schmuki, P. Falaras, Photocatalytic degradation of gas pollutants on self-assembled titania nanotubes, Chem. Phys. Lett. 490 (2010) 58–62.
[14] Xa. Dong, W. Cui, H. Wang, J. Li, Y. Sun, H. Wang, Y. Zhang, H. Huang, F. Dong, Promoting ring-opening efficiency for suppressing toxic intermediates during photocatalytic toluene degradation via surface oxygen vacancies, Sci. Bull. 64 (2019) 669–678.
[15] J. Li, Xa. Dong, G. Zhang, W. Cui, W. Cen, Z. Wu, S.C. Lee, F. Dong, Probing ring-opening pathways for efficient photocatalytic toluene decomposition, J. Mater. Chem. A 7 (2019) 3366–3374.
[16] J. Chen, Z. He, G. Li, T. An, H. Shi, Y. Li, Visible-light-enhanced photo-thermocatalytic activity of ABO3-type perovskites for the decontamination of gaseous styrene, Appl. Catal. B Environ. 209 (2017) 146–154.
[17] W. Zhang, G. Li, H. Liu, J. Chen, S. Ma, T. An, Micro/nano-bubble assisted synthesis of Au/TiO2@ CNTs composite photocatalyst for photocatalytic degradation of gaseous styrene and its enhanced catalytic mechanism, Environ. Sci. Nano 6 (2019) 948–958.
[18] J. Yu, J. Low, W. Xiao, P. Zhou, M. Jaroniec, Enhanced photocatalytic CO(2)-reduction activity of anatase TiO(2) by coexposed {001} and {101} facets, J. Am. Chem. Soc. 136 (2014) 8839–8842.
[19] M. Wang, F. Zhang, X. Zhu, Z. Qi, B. Hong, J. Ding, J. Bao, S. Sun, C. Gao, DRIFTS evidence for facet-dependent adsorption of gaseous toluene on TiO2 with relative photocatalytic properties, Langmuir 31 (2015) 1730–1736.
[20] P. Fu, P. Zhang, J. Li, Photocatalytic degradation of low concentration formaldehyde and simultaneous elimination of ozone by-product using palladium modified TiO2 films under UV254 + 185nm irradiation, Appl. Catal. B Environ. 105 (2011) 220–228.
[21] T. Hashem, M. Zirlewagen, A. Braun, Simultaneous photochemical generation of ozone in the gas phase and photolysis of aqueous reaction systems using one VUV light source, Water Sci. Technol. 35 (1997) 41–48.
[22] X. Xu, P. Wang, W. Xu, J. Wu, L. Chen, M. Fu, D. Ye, Plasma-catalysis of metal loaded SBA-15 for toluene removal: comparison of continuously introduced and adsorption-discharge plasma system, Chem. Eng. J. 283 (2016) 276–284.
[23] D. Conceição, C. Graça, D. Ferreira, A. Ferraria, I. Fonseca, A.B. do Rego, A. Teixeira, L.V. Ferreira, Photochemical insights of TiO2 decorated mesoporous SBA-15 materials and their influence on the photodegradation of organic contaminants, Microporous Mesoporous Mater. 253 (2017) 203–214.
[24] M. Wu, D.Y. Leung, Y. Zhang, H. Huang, R. Xie, W. Szeto, F. Li, Toluene degradation over Mn-TiO2/CeO2 composite catalyst under vacuum ultraviolet (VUV) irradiation, Chem. Eng. Sci. 195 (2019) 985–994.
[25] P. Wei, D. Qin, J. Chen, Y. Li, M. Wen, Y. Ji, G. Li, T. An, Photocatalytic ozonation mechanism of gaseous n-hexane on MO x–TiO 2–foam nickel composite (M = Cu, Mn, Ag): unveiling the role of OH and˙ O 2 −, Environ. Sci. Nano 6 (2019) 959–969.
[26] H. Huang, H. Huang, L. Zhang, P. Hu, X. Ye, D.Y. Leung, Enhanced degradation of gaseous benzene under vacuum ultraviolet (VUV) irradiation over TiO 2 modified by transition metals, Chem. Eng. J. 259 (2015) 534–541.
[27] X. Han, Q. Kuang, M. Jin, Z. Xie, L. Zheng, Synthesis of titania nanosheets with a high percentage of exposed (001) facets and related photocatalytic properties, J. Am. Chem. Soc. 131 (2009) 3152–3153.
[28] M. Wang, F. Zhang, X. Zhu, Z. Qi, B. Hong, J. Ding, J. Bao, S. Sun, C. Gao, DRIFTS evidence for facet-dependent adsorption of gaseous toluene on TiO2 with relative photocatalytic properties, Langmuir 31 (2015) 1730–1736.
[29] Y. Liang, Y. Yang, H. Zhou, C. Zou, K. Xu, X. Luo, T. Yu, W. Zhang, Y. Liu, C. Yuan, A systematic study on the crystal facets-dependent gas sensing properties of anatase TiO2 with designed {010},{101} and {001} facets, Ceram. Int. 45 (2019) 6282–6290.
[30] L. Ren, Y. Li, J. Hou, J. Bai, M. Mao, M. Zeng, X. Zhao, N. Li, The pivotal effect of the

interaction between reactant and anatase TiO2 nanosheets with exposed {0 0 1} facets on photocatalysis for the photocatalytic purification of VOCs, Appl. Catal. B Environ. 181 (2016) 625–634.
[31] S. Fang, Y. Xia, K. Lv, Q. Li, J. Sun, M. Li, Effect of carbon-dots modification on the structure and photocatalytic activity of g-C 3 N 4, Appl. Catal. B Environ. 185 (2016) 225–232.
[32] J. Chen, X. Wu, Y. Gong, P. Wang, W. Li, Q. Tan, Y. Chen, Synthesis of Mn3O4/N-doped graphene hybrid and its improved electrochemical performance for lithium-ion batteries, Ceram. Int. 43 (2017) 4655–4662.
[33] J.Y. Liao, D. Higgins, G. Lui, V. Chabot, X. Xiao, Z. Chen, Multifunctional TiO2-C/MnO2 core-double-shell nanowire arrays as high-performance 3D electrodes for lithium ion batteries, Nano Lett. 13 (2013) 5467–5473.
[34] J. Liu, J. Jiang, C. Cheng, H. Li, J. Zhang, H. Gong, H.J. Fan, Co3O4 Nanowire@ MnO2 ultrathin nanosheet core/shell arrays: a new class of high-performance pseudocapacitive materials, Adv. Mater. 23 (2011) 2076–2081.
[35] X. Lu, M. Yu, G. Wang, T. Zhai, S. Xie, Y. Ling, Y. Tong, Y. Li, H-TiO(2) @MnO(2) //H-TiO(2) @C core-shell nanowires for high performance and flexible asymmetric supercapacitors, Adv. Mater. 25 (2013) 267–272.
[36] S. Deng, T. Meng, B. Xu, F. Gao, Y. Ding, L. Yu, Y. Fan, Advanced MnOx/TiO2 catalyst with preferentially exposed anatase {001} facet for low-temperature SCR of NO, ACS Catal. 6 (2016) 5807–5815.
[37] L. Zhu, J. Wang, S. Rong, H. Wang, P. Zhang, Cerium modified birnessite-type MnO 2 for gaseous formaldehyde oxidation at low temperature, Appl. Catal. B Environ. 211 (2017) 212–221.
[38] J. Hou, Y. Li, M. Mao, L. Ren, X. Zhao, Tremendous effect of the morphology of birnessite-type manganese oxide nanostructures on catalytic activity, ACS Appl. Mater. Interfaces 6 (2014) 14981–14987.
[39] J.C.-C. Yu, V.-H. Nguyen, J. Lasek, J.C.S. Wu, Titania nanosheet photocatalysts with dominantly exposed (001) reactive facets for photocatalytic NOx abatement, Appl. Catal. B Environ. 219 (2017) 391–400.
[40] M. Xue, L. Huang, J.-Q. Wang, Y. Wang, L. Gao, J.-h. Zhu, Z.-G. Zou, The direct synthesis of mesoporous structured MnO2/TiO2 nanocomposite: a novel visible-light active photocatalyst with large pore size, Nanotechnology 19 (2008) 185604.
[41] H. Jun, B. Im, J.Y. Kim, Y.-O. Im, J.-W. Jang, E.S. Kim, J.Y. Kim, H.J. Kang, S.J. Hong, J.S. Lee, Photoelectrochemical water splitting over ordered honeycomb hematite electrodes stabilized by alumina shielding, Energy Environ. Sci. 5 (2012) 6375–6382.
[42] F. Yam, K. Beh, S. Ng, Z. Hassan, The effects of morphological changes on the vibrational properties of self-organized TiO2 nanotubes, Thin Solid Films 520 (2011) 807–812.
[43] Y.-K. Hsu, Y.-C. Chen, Y.-G. Lin, L.-C. Chen, K.-H. Chen, Reversible phase transformation of MnO 2 nanosheets in an electrochemical capacitor investigated by in situ Raman spectroscopy, Chem. Commun. 47 (2011) 1252–1254.
[44] F. Tian, Y. Zhang, J. Zhang, C. Pan, Raman spectroscopy: a new approach to measure the percentage of anatase TiO2 exposed (001) facets, J. Phys. Chem. C 116 (2012) 7515–7519.
[45] W. Zhao, Y. Feng, H. Huang, P. Zhou, J. Li, L. Zhang, B. Dai, J. Xu, F. Zhu, N. Sheng, A novel Z-scheme Ag3VO4/BiVO4 heterojunction photocatalyst: study on the excellent photocatalytic performance and photocatalytic mechanism, Appl. Catal. B Environ. 245 (2019) 448–458.
[46] Y. Zhu, X. Zhao, J. Li, H. Zhang, S. Chen, W. Han, D. Yang, Surface modification of hematite photoanode by NiFe layered double hydroxide for boosting photoelectrocatalytic water oxidation, J. Alloys. Compd. 764 (2018) 341–346.
[47] T. Giannakopoulou, I. Papailias, N. Todorova, N. Boukos, Y. Liu, J. Yu, C. Trapalis, Tailoring the energy band gap and edges' potentials of g-C3N4/TiO2 composite photocatalysts for NOx removal, Chem. Eng. J. 310 (2017) 571–580.
[48] H. Huang, D.Y. Leung, G. Li, M.K. Leung, X. Fu, Photocatalytic destruction of air pollutants with vacuum ultraviolet (VUV) irradiation, Catal. Today 175 (2011) 310–315.
[49] J. Wang, P. Rao, W. An, J. Xu, Y. Men, Boosting photocatalytic activity of Pd decorated TiO2 nanocrystal with exposed (001) facets for selective alcohol oxidations, Appl. Catal. B Environ. 195 (2016) 141–148.
[50] J.J. Murcia, M.C. Hidalgo, J.A. Navío, V. Vaiano, D. Sannino, P. Ciambelli, Cyclohexane photocatalytic oxidation on Pt/TiO2 catalysts, Catal. Today 209 (2013) 164–169.
[51] X. Li, X. Zou, Z. Qu, Q. Zhao, L. Wang, Photocatalytic degradation of gaseous toluene over Ag-doping TiO2 nanotube powder prepared by anodization coupled with impregnation method, Chemosphere 83 (2011) 674–679.
[52] Y.-T. Wu, Y.-H. Yu, V.-H. Nguyen, K.-T. Lu, J.C.-S. Wu, L.-M. Chang, C.-W. Kuo, Enhanced xylene removal by photocatalytic oxidation using fiber-illuminated honeycomb reactor at ppb level, J. Hazard. Mater. 262 (2013) 717–725.
[53] H.-H. Tseng, M.-C. Wei, S.-F. Hsiung, C.-W. Chiou, Degradation of xylene vapor over Ni-doped TiO2 photocatalysts prepared by polyol-mediated synthesis, Chem. Eng. J. 150 (2009) 160–167.
[54] S.-B. Yang, H.-H. Chun, R.J. Tayade, W.-K. Jo, Iron-functionalized titanium dioxide on flexible glass fibers for photocatalysis of benzene, toluene, ethylbenzene, and o-xylene (BTEX) under visible-or ultraviolet-light irradiation, J. Air Waste Manage. Assoc. 65 (2015) 365–373.
[55] D. Xia, W. Xu, L. Hu, C. He, D.Y. Leung, W. Wang, P.K. Wong, Synergistically catalytic oxidation of toluene over Mn modified g-C3N4/ZSM-4 under vacuum UV irradiation, J. Hazard. Mater. 349 (2018) 91–100.
[56] J. Chen, Z. He, Y. Ji, G. Li, T. An, W. Choi, · OH radicals determined photocatalytic degradation mechanisms of gaseous styrene in TiO2 system under 254 nm versus 185 nm irradiation: combined experimental and theoretical studies, Appl. Catal. B Environ. (2019) 117912.
[57] J. Kim, C.W. Lee, W. Choi, Platinized WO3 as an environmental photocatalyst that generates OH radicals under visible light, Environ. Sci. Technol. 44 (2010) 6849–6854.
[58] T. Ochiai, K. Masuko, S. Tago, R. Nakano, Y. Niitsu, G. Kobayashi, K. Horio, K. Nakata, T. Murakami, M. Hara, Development of a hybrid environmental purification unit by using of excimer VUV lamps with TiO2 coated titanium mesh filter, Chem. Eng. J. 218 (2013) 327–332.
[59] J.F. García-Araya, F.J. Beltrán, A. Aguinaco, Diclofenac removal from water by ozone and photolytic TiO2 catalysed processes, J. Chem. Technol. Biotechnol. 85 (2010) 798–804.
[60] H. Einaga, A. Ogata, S. Futamura, T. Ibusuki, The stabilization of active oxygen species by Pt supported on TiO2, Chem. Phys. Lett. 338 (2001) 303–307.
[61] Y. Liu, W. Yang, P. Zhang, J. Zhang, Nitric acid-treated birnessite-type MnO2: an efficient and hydrophobic material for humid ozone decomposition, Appl. Surf. Sci. 442 (2018) 640–649.
[62] J. Jia, P. Zhang, L. Chen, Catalytic decomposition of gaseous ozone over manganese dioxides with different crystal structures, Appl. Catal. B Environ. 189 (2016) 210–218.
[63] Y. Shu, J. Ji, Y. Xu, J. Deng, H. Huang, M. He, D.Y. Leung, M. Wu, S. Liu, S. Liu, Promotional role of Mn doping on catalytic oxidation of VOCs over mesoporous TiO2 under vacuum ultraviolet (VUV) irradiation, Appl. Catal. B Environ. 220 (2018) 78–87.